

Highly Reliable Flexible Device With Charge Compensation Layer

Hyojung Kim

OLED Business Samsung Display Co., Ltd.

Jongwoo Park

OLED Business Samsung Display Co., Ltd.

Taeyoung Khim

OLED Business Samsung Display Co., Ltd.

Hyuncheol Hwang

OLED Business Samsung Display Co., Ltd.

Jungmin Park

Sungkyunkwan University

Chanhee Han

Sungkyunkwan University

Jongmin Yoo

Sungkyunkwan University

Dongbin Kim

Sungkyunkwan University

Jangkun Song

Sungkyunkwan University

Byoungdeog Choi (✉ bdchoi@skku.edu)

Sungkyunkwan University

Research Article

Keywords: flexible, SiCOH, abnormal, reliable

Posted Date: January 7th, 2022

DOI: <https://doi.org/10.21203/rs.3.rs-1201021/v1>

License: © ⓘ This work is licensed under a Creative Commons Attribution 4.0 International License.

[Read Full License](#)

Version of Record: A version of this preprint was published at ACS Applied Materials & Interfaces on March 2nd, 2022. See the published version at <https://doi.org/10.1021/acsami.1c24820>.

Abstract

Flexible devices fabricated with polyimide (PI) substrate are crucial for foldable, rollable, or stretchable products in various applications. However, inherent technical challenges remain in mobile charge induced device instabilities and image retention, significantly hindering future technologies. We introduced a new barrier material, SiCOH, into the backplane of amorphous indium-gallium-zinc-oxide (a-IGZO) thin-film transistors (TFTs) that were then implemented into production-level flexible panels. We found that the SiCOH layer effectively compensates the surface charging induced by fluorine ions at the interface between the PI substrate and the barrier layer under bias stress, thereby preventing abnormal positive V_{th} shifts and image disturbance. The a-IGZO TFTs, metal-insulator-metal (MIM), and metal-insulator-semiconductor (MIS) capacitors with the SiCOH layer demonstrate reliable device performance, V_{th} shifts, and capacitance changes with an increase in the gate bias stress. A flexible device with SiCOH enables the suppression of abnormal V_{th} shifts associated with PI and plays a vital role in the degree of image sticking phenomenon. This work provides new inspirations to creating much improved process integrity and paves the way for expediting versatile form-factors.

Introduction

Unlike rigid electronic devices, flexible devices have a plastic substrate capable of stretching and folding into adjustable shapes due to new form factors driven by the development of life-convenient features in various applications^{1,2}. Such applications include display devices³, wearable sensors⁴, flexible batteries^{5,6}, medical fields^{7,8}, and artificial intelligence-based electronic skin^{9,10}. Since flexible electronics must withstand significant mechanical strains due to their complex shapes, excellent physical and electrical material properties and reliability are inevitable^{11,12}. Various polymeric materials have been explored as the substrate material for flexible devices^{13,14}. However, a few materials were found suitable mainly due to the process limitation for flexible substrates associated with process temperature, lithography resolution and substrate cleanliness¹⁵. One of the feasible materials is polyimide (PI), which provides high glass transition temperature, low coefficient of thermal expansion, and strong chemical resistance^{16,17}. In particular, fluorinated PI films are widely adopted in mainstream flexible electronics because of their excellent optical transparency and high thermal conductivity^{18,19}.

When thin-film transistors (TFTs) of flexible devices are fabricated, a barrier film underneath the channel must be deposited on the PI substrate. The barrier film intends to block moisture absorption and support the integrity as a mechanical buffer. Considering process integrity, SiO_2 or Al_2O_3 is extensively used as a barrier layer²⁰. TFT has a broad range of applications in displays and flexible devices, and several channel materials have been extensively studied, including low-temperature polycrystalline silicon (LTPS)^{21,22}. However, we reported that the LTPS and amorphous indium-gallium-zinc-oxide (a-IGZO) TFT fabricated on the PI substrate had abnormal V_{th} behaviors under the gate bias stress^{23,24}. When the bias stress is applied to the transistor, fluorine ions (F^-) are prone to be trapped at the SiO_2 barrier and PI

interface²⁵. Such PI charging is detrimental, particularly for flexible electronic products fabricated with the PI substrate. It has been reported that charge-induced V_{th} shifts in TFTs on PI substrates lead to residual images that ultimately impact display image quality^{26,27}. Especially, commonly used TFTs including LTPS and a-IGZO TFT that adopt new features such as low frequency and always-display-on are susceptible to charge-induced degradation and image retention^{25,28}. One of the feasible solutions proposes a metal layer deposition underneath the channel above the PI substrate for blocking PI charging^{29,30}. However, the details about the blocking mechanism have not been fully investigated. Despite being a possible solution, the blocking metal layer would limit flexibility and require an additional mask layer and the investment of sputtering equipment, which is not beneficial for cost-effective manufacturing and production.

This study proposes a new barrier layer of SiCOH that can effectively compensate for F^- induced charging for a flexible a-IGZO device with the PI substrate. A solution to fluorine-induced device instabilities is to integrate a SiCOH layer underneath the SiO_2 barrier layer, hence creating a dual barrier layer of $SiO_2/SiCOH$. Multifaceted approaches such as a-IGZO TFT devices, the metal-insulator-metal (MIM), and the metal-insulator-semiconductor (MIS) capacitors have been taken to address electrical and display performance disturbance issues using the current-voltage (I-V) and capacitance-voltage (C-V) characteristics and physical characterization such as Kelvin probe force microscopy (KPFM) and secondary ion mass spectrometry (SIMS). We found that a-IGZO devices with the SiCOH deposited on the PI substrate demonstrate reliable V_{th} shifts and display image quality despite even increasing bias stressing. We explicitly observed the charging phenomenon of the PI at the interface between PI and $SiO_2/SiCOH$ and elucidated the effect of the SiCOH layer and charge compensation for F^- from PI substrates under the bias. Accordingly, the SiCOH layer traps F^- and suppresses V_{th} shifts and image retention of flexible devices. Hence, flexible devices with the SiCOH layer help cultivate the prosperities of new applications in portable and wearable electronics.

Results

I_D-V_G characteristics of TFTs before and after bias temperature stress

Figure 1a shows the structure of a rigid organic light-emitting diode (OLED) display panel manufactured on a glass substrate and a flexible OLED display panel manufactured on a PI substrate. For the two types of panels, a-IGZO TFT was used as the driving device, and OLED was used as the light emitting device. A device that has been processed up to TFT is called a backplane. Figures 1b, c, and d show the three different a-IGZO TFT structures used in this study. Devices A and B have the same barrier structure of SiO_2 and different substrates of glass and PI, respectively. However, Devices B and C have the same substrate with PI, but the barrier structure is different with SiO_2 and $SiO_2/SiCOH$, respectively. The $SiO_2/SiCOH$ bilayer is the barrier structure proposed in this paper. Figures 1d, e, and f show the change of

drain current (I_D)-gate voltage (V_G) of the three devices before and after negative bias temperature stress (NBTS) that applies an electric field of -1 MV/cm to the gate electrode at 70°C for 4,000 s. After NBTS, the V_{th} shift (ΔV_{th}) for Devices A, B, and C is (-0.36, +0.45, and -0.25) V, respectively. Note that Devices A and C have the same negative V_{th} shift, while Device B has a positive V_{th} shift. Supplementary Table 1 summarizes the specific numbers of changes in the transfer parameters of TFTs before and after NBTS. The positive V_{th} shift under NBTS is an abnormal phenomenon, which is hard to understand with the generally accepted degradation models such as the reaction–diffusion model³¹. The general degradation models focus on the events occurring at the semiconducting channel and gate insulator layer interface. Furthermore, the interface defect densities (N_{it}) of these three devices, extracted through the subthreshold swing (SS) method, were very similar before and after NBTS, which indicates that the N_{it} between channel and gate insulator of these devices are similar before and after NBTS. Considering these experimental results of Devices A and B, it can be easily inferred that the PI substrate is involved in the abnormal degradation of Device B. A previous study found that the cause of the abnormal V_{th} behavior in flexible TFTs was that F^- was generated from PI, and charging occurred at the interface between PI and the barrier²⁵. Such abnormal deterioration of electronic devices may cause fatal problems in the performance of flexible electronic products. For example, as depicted in Supplementary Fig. 6, an issue of image quality occurs in which the luminance of the black pattern decreases due to this abnormal deterioration phenomenon of TFTs in flexible OLED displays using the PI substrates. Supplementary Figure 6d shows the image sticking failure caused by a positive V_{th} shift of transistors on the flexible OLED display panels fabricated over PI substrate and single layer (SiO_2) barrier, which has the same structure as Device B.

Electrical and physical characteristics of the MIM and MIS capacitor

Two kinds of MIM capacitors were manufactured, and experiments were carried out to identify the cause of the different V_{th} behaviors of Device B and Device C after gate bias stress application. As shown in Figs. 2a and b, the insulators used for the MIM capacitor have the same structure and manufacturing process conditions as the TFTs used in Figs. 1b and c. Supplementary Table 2 summarizes the material and electrical characteristic parameters of the insulator used in the MIM capacitors extracted through scanning electron microscopy (SEM) and C–V measurements shown in Supplementary Fig. 1 and Supplementary Fig. 2, respectively. To analyse the effect of stress conditions on the PI substrate, three distinct voltages of (-10, -20, and -30) V were applied to the top electrode at a temperature of 70°C for 10 minutes. The I–V and C–V measurements confirmed the changes in the electrical characteristics of the MIM capacitor before and after stress. Supplementary Figure 3 is the I–V plot as a function of the voltage applied to each MIM capacitor. Figure 2c shows the normalized change of the leakage current of the MIM capacitor according to the voltage applied to the top electrode. The MIM A capacitor (Al/SiO₂/PI/Al), which has the same barrier structure as Device B, exhibited higher leakage current fluctuations after NBTS than MIM B capacitor (Al/SiO₂/SiCOH/PI/Al), which has the same structure as Device C. This result implies that the insulator structure in MIM B is more stable under the bias stress than that of MIM A. The

phenomenon behind the leakage current can be explained as follows. The hole carriers inject into the PI and break chemical bonds in the organic chains. Then, the ions such as F^- generated from the broken bonds of the chains act as charged defects and increase the leakage current through the capacitors^{27,32}. Figure 2d shows the increase in the volume resistivity of each MIM capacitor after NBTS. Here, a decrease in the resistivity of the PI can enhance the free movement of mobile charges such as charged ions, in the PI substrate. Figures 2e and f show the change in capacitance and charge density, respectively, according to the voltage application of the two MIM capacitors after NBTS. The capacitance increase indicates that the capability of containing charged ions within the interface increases. The increasing charge density of MIM capacitors infers that the number of charges trapped within the interface between barrier and PI increases. The trapped charges within the interface induce an electric field that influences the electrical properties of the devices fabricated above. Comparing the changes in leakage current, volume resistivity, total capacitance, and charge density under the bias stress, it is confirmed that MIM B is more stable than MIM A in electrical properties. Overall, these results indicate that the devices having the same barrier structure as MIM B may be more robust to an external disturbance such as an electric field. The electric field generated by trapped charges can be extracted by converting the capacitance change of the PI film into an electric charge (Supplementary Fig. 4), which implies that the change in charge density represents the generation of substrate bias. During the NBTS evaluation, it was estimated that the positive V_{th} shift occurred due to electron accumulation in the semiconducting bulk layer, rather than hole trapping at the gate insulator and channel interface, as the voltage stress increased.

Furthermore, three MIS capacitors imitating the barrier and substrate structure of Devices A, B, and C were fabricated and named MIS A, MIS B, and MIS C, respectively. Each MIS capacitor has the barrier and substrate structure with Al/ Al_2O_3 / a-IGZO/ SiO_2 /glass for MIS A, Al/ Al_2O_3 / a-IGZO/ SiO_2 /PI for MIS B, and Al/ Al_2O_3 / a-IGZO/ SiO_2 /SiCOH/PI for MIS C, and mobile charge measurement was performed. Figures 3a, b, and c illustrate experimental configurations of the three MIS capacitors using C-V measurements. Stress voltage was applied to the Al electrode with the substrate grounded as shown in Figs. 3a, b, and c to detect the effect of mobile charge within the PI in the MIS devices. 1 MV/cm electric field was applied to the upper electrode at 200 °C for 600 s to measure the mobile charges. Then the C-V plot was extracted by sweeping the voltage applied to the upper gate electrode. After that, the field was applied to the upper gate electrode at 200 °C for 600 s by changing only the polarity in the measurement method mentioned above, and then the C-V plots were measured. Figure 3g represents the microscopy image of the MIS capacitor for the C-V measurement. Figures 3d, e, and f show the results of the mobile charge measurement of each MIS device. The mobile charge analysis results of the three devices confirmed that the differences between the measurement results before and after applying the gate voltage of -/+1 MV for MIS A and MIS C were very similar. However, in the case of MIS B, it is evident that the flatband voltage (V_{FB}) difference was very large when the -1 MV and the +1 MV were applied. ΔV_{FB} and mobile charges can be calculated by $Q_m = -C_{total} \times \Delta V_{FB}$, where Q_m is the mobile charge density and $C_{total} = 1/(1/C_{gate\ insulator} + 1/C_{barrier} + 1/C_{PI})$. From this equation, we can confirm that as ΔV_{FB} increases, the mobile charge increases.

Previous studies have reported that the impurity mobile ions in the gate insulator layer are mainly responsible for the degradation of transistors³¹. However, because the only difference between MIS A and MIS B is the substrate material, it can be inferred that the mobile charges within the PI substrate play a major role in the degradation phenomena. Figure 3h shows a schematic of the charging phenomenon of the MIS capacitor when measuring the mobile charge. When a negative field is applied to the upper electrode, negative ions lead to positive polarity on the upper side of the PI. Electrons are accumulated at the bottom of the channel layer to prevent channel formation, leading to a positive shift of the C–V curve. However, the mobile charge measurement result of MIS C matched the MIS A measurement result made on a glass substrate. These results confirm once again that the barrier structure proposed in this study can play a vital role in preventing the charging phenomenon caused by the mobile charges inside the PI substrate.

Using KPFM, we can directly observe the mobile charges and intuitively confirm the charging phenomenon of the PI interface and the effect of the SiCOH film in terms of charging compensation. KPFM can also quantify the contact potential difference (CPD) between the sample surface and the tip to confirm the presence or absence of charging for each layer of the device^{34–38}. Supplementary Figs. 5a-c and Fig. 5d illustrate the concept of the KPFM measurement method and the detailed sample preparation procedure for KPFM measurement used in this study, respectively. The CPD between the tip and the device was measured by moving across the atomic force microscopy (AFM) tip including the MIM capacitor structure from the glass to the resin sample, as shown in Figs. 4a and b. The measurements were performed before and after applying -10 V to the top electrode for 10 min for each of the two types of MIM capacitors: MIM A and MIM B. Figures 4c, d, and e show the surface potential profiles before and after applying bias for MIM A. It can be observed that after the bias is applied, the surface potential increases from the SiO₂/PI interface to the PI films. It can be reasonable to suggest that negative charges in PI film exist, based on the fact that the CPD is linearly proportional to $\phi_{\text{tip}} - \phi_{\text{sample}}$ ³⁹. However, the MIM B showed little change in CPD before and after applying bias, as shown in Figs. 4f, g, and h. This conclusive evidence suggests that the SiCOH film as a barrier layer can effectively remove the PI charging phenomenon in the flexible devices using the PI substrate.

Physical analysis and PI charging compensation mechanism

The optimal SiCOH film formation conditions were found by varying the plasma power during the PECVD deposition. Figure 5a shows the Fourier transform infrared (FTIR) spectroscopy measurement results for the SiCOH single film deposited by varying the plasma power for (60 and 100) W. The peak at (1,300–1,240) cm⁻¹ in the entire wavelength range comes from the Si–CH₃ bond. From (1,240 to 950) cm⁻¹, the peak occurs in the Si–O related stretching vibration mode. The wide absorption band between (950 and 650) cm⁻¹ corresponds to the Si–(CH₃)_x (x = 1, 2, 3) bending vibration⁴⁰. Figure 5b shows the FTIR spectra fitted with five peaks concentrated at (805, 960, 1,007, 1,136, and 1,250) cm⁻¹. Silicon-related peaks were normalized, and the integrated area of each peak was divided into the total integrated area.

From this result, we can confirm that when the SiCOH film is deposited by the PECVD process, the Si–O bond decreases, and the Si–CH₃ bond increases as the plasma power decreases. In this study, the SiCOH film was deposited under a plasma power of 60 W. To determine the causative factors that induce the charging effect in the actual PI before/after bias temperature stress, we conducted a physical analysis. Figures 5c and d show the SIMS results before and after NBTS application of two types of capacitors, MIM A (Al/SiO₂/PI/Al) and MIM B (Al/SiO₂/SiCOH/PI/Al) capacitors. It can be seen that the F[−] from PI is relatively highly accumulated at the SiO₂/PI interface of the MIM A capacitor after NBTS. These accumulated F[−] can act as ionized charges and affect the characteristics of TFTs and other devices fabricated on the PI substrate^{41,42}. However, MIM B had no changes in the amount of F[−] accumulation at the barrier and PI interface even after NBTS. This is due to the F-binding with Si in the SiCOH film since the electron affinity of F (328 KJ/mol) is higher than that of C (122 KJ/mol). Figure 5e summarizes the step-by-step mechanism of how the SiCOH film consumes F[−] from PI. When NBTS is applied to the MIM capacitor, F[−] from PI are accumulated at the barrier and PI interface (step 1). However, the Si–CH₃ bond in the SiCOH film is broken by the bias temperature stress, and F[−] with higher electron affinity binds to Si to form a Si–F bond, neutralizing the negative charge from F[−] and ultimately suppressing the surface charging phenomenon (step 2). Carbon that is not bonded can be replaced by C–C or C–H bonding, and since this is a nonpolar bond, the charging effect can be prevented⁴³.

Stable flexible display performance verification

Figure 6a is an actual picture of the flexible display panel used in this study. The V_{th} shift after NBTS of the TFTs in Fig. 1 was obtained from a total of 15 samples (5 samples per device), and the V_{th} shift is exhibited in the box plot in Fig. 6b. As opposed to Device A and C that exhibit negative V_{th} shifts, Device B exhibits V_{th} shifts that move in the positive direction. This abnormal positive V_{th} shift of the TFT device may cause image sticking in the flexible panel. One of the metrics that can measure display panel quality is the display image sticking evaluation. Image sticking refers to a phenomenon in which an image remains visible even after the next frame is written, thereby hindering the visibility of the succeeding image²⁴. Supplementary Figure 5a shows the evaluation method of display image sticking. The luminance is measured at the first 64-gray pattern, which is aged for a certain time under the pattern where the black/white pattern intersects, and the luminance is measured again at the 64-gray pattern. The level at which the luminance exceeds a certain level in the late 64-gray pattern compared to the initial 64-gray pattern is evaluated as an afterimage time value. Figure 6c shows the image sticking evaluation result of the panels manufactured on Device A, B, and C. It can be confirmed that the panel manufactured on Device C has the same level of image sticking as the panel manufactured on Device A, while the panel manufactured on Device B exhibits very severe image sticking. Figure 6d shows the results of manufacturing an actual OLED display on Devices A, B, and C, initially aging it from 64-gray patterns to a chess pattern, and then measuring the panel state with a camera in the state of the 64 gray pattern. The panel manufactured on Device B confirmed that the part that had been aged with a black pattern looked darker and was recognized as image sticking. Supplementary Figures 5c and d show that the specific behavior (positive V_{th} shift) in the TFT device can induce this image sticking.

These results represent that the operating current of devices manufactured on PI can flow differently than expected, which can adversely affect performance of flexible electronics. In addition, it is shown that the SiCOH film presented in this study can suppress the charging phenomenon of PI and the image sticking problem by introducing the SiCOH film as a barrier. The SiCOH layer that can prevent the PI charging effect is expected to apply to all flexible devices.

Conclusions

This work demonstrates a PI-substrate-based flexible device that overcomes the bias-induced surface charging instability by introducing a SiCOH film as a barrier layer that provides better electrical characteristics via mobile charge compensation. Although the PI has attractive benefits of material properties, flexible devices with the PI substrate suffer from fluorine-induced surface charging. F^- will accumulate in the PI and barrier interface particularly under bias conditions, unless an additional layer, either organic or inorganic material, is implemented for process integrity. To resolve the PI-charging-induced disturbance and instability of flexible devices, SiCOH is chosen as a barrier layer and adopted into the interface between SiO_2 and PI as one of the feasible knobs. Results show that flexible devices with SiCOH layer have stable and reliable performance without any disturbances attributed to mobile charges associated with PI. Indeed, the physical analysis of KPFM and SIMS elucidates that the SiCOH layer helps garner F^- stemmed from PI substrate and serves as a charged ion compensation layer. SiCOH effectively shields TFTs with the PI substrates from charging induced instability even with elevated gate bias. Furthermore, to confirm the benefits observed and the feasibility of our research in terms of production applicability, we fabricated a flexible OLED display panel with a SiCOH layer. We believe that even if an extreme form factor launches, our proposed structure's robustness and mechanical flexibility can ensure enriched performance and contribute to production-worthy technologies in future.

Methods

Device fabrication. We used three top gate staggered TFTs consisting of substrates (PI, Glass) and thereon buffer layers (SiO_2 , $SiO_2/SiCOH$). The $5\mu m$ thick PI film was coated in an air atmosphere at a speed of 1000 RPM for 60 s. After soft bake at $80\text{ }^\circ C$ for 30 min, it was subjected to hard bake at $460\text{ }^\circ C$ for 2 h. The thickness of the final PI film is approximately $5\text{ }\mu m$. A SiO_2 thin film as a buffer layer was deposited on both PI and glass substrate and a $SiO_2/SiCOH$ double layer was deposited on PI by PECVD method. The total thickness of the buffer layers was controlled to 300 nm for both the SiO_2 and $SiO_2/SiCOH$ layers. Here, the precursors used for the SiO_2 and the SiCOH film were SiH_4 and TTMSS (Sigma Aldrich, 97% purity, boiling point: $(103-106)\text{ }^\circ C$ at 2 mmHg), respectively. SiCOH film conditions were selected by varying the plasma power during PECVD deposition. Then, a sputter-deposited Mo (50 nm) layer was patterned by photolithography to form source-drain electrodes. On top of that, a 30 nm thick a-IGZO film was deposited by RF/DC sputtering method with the target composition ratio of In:Ga:Zn:O = 1:1:1:4, followed by a patterning process to finalize the active layer. A layer of 100 nm of Al_2O_3 on patterned on the active layer was deposited by atomic layer deposition method at a substrate

temperature of 150 °C using TMA(Al(CH₃)₃) as a precursor and O₂ plasma as a reactant to form a gate insulator. After the contact holes were formed on the Al₂O₃ insulator using photolithography, the annealing process was carried out at 180 °C for 40 min to activate the a-IGZO layer. Subsequently, a 50 nm layer of Mo was deposited using a DC sputtering method and patterned to form source-drain contacts and gates.

Two types of MIM capacitors, Al/SiO₂/PI/Al and Al/SiO₂/SiCOH/Al with the same thickness and process conditions as the insulator used as a barrier, were manufactured and used in the experiment.

Flexible display panel fabrication. We fabricated three types of flexible OLED panels with different barrier layers (SiO₂ and SiO₂/SiCOH) deposited on top of either PI or glass substrate. After using the aforementioned a-IGZO TFT as a backplane, OLED was deposited as a light emitting layer through a thermal evaporation process. SiO₂/Si₃N₄/SiO₂ was deposited as a thin film encapsulation (TFE) layer to prevent the penetration of moisture into the organic material. A polarizer was attached to the TFE film, so that light was emitted in a specific direction. A display driver IC (DDI) package was implemented to drive the display pixels. The DDI and flexible printed circuit board (FPCB) were installed so that they could interoperate with external electrical signals, and finally, the three types of flexible OLED display panels with different substrate and barrier structures were produced.

Electrical characterization. I–V and C–V measurements were carried out for the initial and post-stress characteristics of the devices. An Agilent B1500A Semiconductor Analyzer was used for I–V measurement, and an Agilent E4980A LCR meter was used for C–V measurement. For the flexible a-IGZO TFTs transfer curve, each gate voltage was swept from (–10 to 5) V with a drain voltage bias of 5.1 V. ΔV_{th} was extracted using the threshold current method, in which a specific gate voltage with a drain current (I_D) of 10 nA × W/L under a drain voltage of 5.1 V (saturation region) was measured before (initial) and after (4,000 s) NBTS. The ΔV_{th} was then calculated by subtracting the initial V_{th} from the post-stress V_{th} . SS was extracted through the following formula:

$$SS = \left(\frac{dV_G}{d\log I_D} \right)_{max}$$

Declarations

Data Availability

All data related to this paper can be requested from the corresponding author upon reasonable request.

Acknowledgements

This research was funded and conducted under the Competency Development Program for Industry Specialists of the Korean Ministry of Trade, Industry and Energy (MOTIE), operated by Korea Institute for

Ethics declarations

Competing interests

The authors declare no competing interests.

Contributions

H. J. K., & J. W. P conceived and designed the experiments. H. J. K., J. M. P., & T. Y. K., fabricated the devices. H. J. K., T. Y. K. performed the physical tests and analyzed the results. H. C. H., C. H. H., J. M. Y., J. M. P., & D. B. K. carried out the electrical measurements and device modeling. J. W. P., J. K. S., & B. D. C. supervised the project.

References

1. Dong, K. et al. Fiber/Fabric-Based Piezoelectric and Triboelectric Nanogenerators for Flexible/Stretchable and Wearable Electronics and Artificial Intelligence. *Adv. Mater.* **32**, 1902549 (2020).
2. Gao, L. Flexible Device Applications of 2D Semiconductors. *Small* **13**, 1603994 (2017).
3. Liang, J. et al. Elastomeric polymer light-emitting devices and displays. *Nat Photonics.* **7**, 817–824 (2013).
4. Rogers, J. A., Someya, T., Huang, Y. Materials and mechanics for stretchable electronics. *Science* **327**, 1603 (2010).
5. Chen, Z. et al. A three-dimensionally interconnected carbon nanotube-conducting polymer hydrogel network for high-performance flexible battery electrodes. *Adv Energy Mater.* **4**, 1400207 (2014).
6. Lin, H. et al. Twisted aligned carbon nanotube/ silicon composite fiber anode for flexible wire-shaped lithium-ion battery. *Adv Mater.* **26**, 1145–1303 (2014).
7. Kenry., Yeo, J. C., Lim, C. T. Emerging flexible and wearable physical sensing platforms for healthcare and biomedical applications. *Microsyst Nanoeng.* **2**, 16043 (2016).
8. Lacour S. P. et al. Flexible and stretchable micro-electrodes for in vitro and in vivo neural interfaces. *Med Biolog Eng Comput.* **48**, 945–954 (2010).
9. Park, J. H. et al. Giant tunneling piezoresistance of composite elastomers with interlocked microdome arrays for ultrasensitive and multimodal electronic skins. *ACS Nano* **8**, 4689–4697 (2014).
10. Chortos, A. et al. Pursuing prosthetic electronic skin. *Nat Mater.* **15**, 937–950 (2016).
11. Akinwande, D. et al. Two-dimensional flexible nanoelectronics. *Nat Commun.* **5**, 5678 (2014).

12. Zou, M. et al. Flexible devices: from materials, architectures to applications. *J. Semicond.* **39**, 011010 (2017).
13. Han, Su-Ting, et al. An overview of the development of flexible sensors. *Adv. Mater.* **29**, 1700375. (2017).
14. Lu, Qing-Hua, and Feng Zheng. Polyimides for electronic applications. *Adv. Poly. Mater.* 195–255. (2018).
15. Malik, Ankit, and Balasubramanian Kandasubramanian. Flexible polymeric substrates for electronic applications. *Polymer Reviews* **58**, 630–667 (2018).
16. Fortunato, G. et al. Polysilicon thin-film transistors on polymer substrates. *Mater. Sci. Semicond. Process.* **15**, 627–641 (2012).
17. Chen, J., Liu, C. Technology advances in flexible displays and substrates. *IEEE Access* **1**, 150–158 (2013).
18. Xiao, T., Fan, X., Fan, D. & Li, Q. High thermal conductivity and low absorptivity/emissivity properties of transparent fluorinated polyimide film. *Polym. Bull.* **74**, 4561–4575 (2017).
19. Hougham, G. et al. Polarization Effects of Fluorine on the Relative Permittivity in Polyimides. *Macromolecules* **27**, 5964–5971 (1994).
20. Sarma, K. R. *Flexible Displays: Substrate and TFT Technology Options and Processing Strategies – from Handbook of Visual Display Technology. In: Chen, J. (eds.)* (Springer, Switzerland, 2016).
21. Hong, J. H. et al. 9.1-inch stretchable AMOLED display based on LTPS technology. *SID Symp. Dig. Tech.* **25**, 1383-1385 (2017).
22. Myny, K. The development of flexible integrated circuits based on thin-film transistors. *Nat. Electron.* **1**, 30–39 (2018).
23. Kim, J. H. et al. Vt behaviors of LTPS-TFT fabricated on PI substrate for flexible applications. *SID Symp. Dig. Tech.* **48**, 1773-1776 (2017).
24. Han, K. L. et al. Comparative study on hydrogen behavior in InGaZnO thin film transistors with a SiO₂/SiN_x/SiO₂ buffer on polyimide and glass substrates. *Electron. Mater. Lett.* **14**, 749–754 (2018).
25. Kim, H. J. et al. Threshold voltage instability and polyimide charging effects of LTPS TFTs for flexible displays. *Sci. Rep.* **11**, 8387 (2021).
26. Kim, H. J. et al. Effects of channel doping on flexible LTPS TFTs: density of state, generation lifetime, and image sticking. *SID Symp. Dig. Tech.* **51**, 1383-1385 (2020).
27. Kim, H. J. et al. Charging compensation layer on polyimide for enhanced device stability in flexible technology. *Electron. Mater. Lett.* **17**, 215–221 (2021).
28. Kim, H. J. et al. Effects of polyimide curing on image sticking behaviors of flexible displays. *Sci. Rep.* **11**, 21805 (2021).
29. Lee, J. S. et al. Alleviation of abnormal NBTI phenomenon in LTPS TFTs on polyimide substrate for flexible AMOLED. *J. Soc. Inf. Display.* **28**, 333–341 (2020).

30. Kinoshita, T. et al. Requirement of a polyimide substrate to achieve high thin-film-transistor reliability. *SID Symp. Tech. Dig. Papers.* **49**, 888-891 (2018).
31. RaJa, J. et al. Negative gate-bias temperature stability of N-doped InGaZnO active-layer thin-film transistors. *Appl. Phys. Lett.* **102**, 083505 (2013).
32. Lee, Y. K. et al. Study of hysteresis behavior of charges in fluorinated polyimide film by using capacitance-voltage method. *Mod. Phys. Lett. B.* **20**, 445–449 (2006).
33. Schroder, D. K. *Semiconductor Material and Device Characterization* (Wiley, 2006).
34. Kim, Y. S. et al. Origin of surface potential change during ferroelectric switching in epitaxial PbTiO₃ thin films studied by scanning force microscopy. *Appl. Phys. Lett.* **94**, 032907 (2009).
35. Hoppe, H. et al. Kelvin Probe Force Microscopy Study on Conjugated Polymer/Fullerene Bulk Heterojunction Organic Solar Cells. *Nano Lett.* **5**, 269–274 (2005).
36. Hallam, T. et al. A scanning Kelvin probe study of charge trapping in zone-cast pentacene thin film transistors. *Nanotechnology* **20**, 025203 (2008).
37. Liu, M., Li, G. Electrical characterization of single-walled carbon nanotubes in organic solar cells by Kelvin probe force microscopy. *Appl. Phys. Lett.* **96**, 083302 (2010).
38. Melitz, W. et al. Kelvin probe force microscopy and its application. *Surface science reports* **66**, 1–27 (2011).
39. Nonnenmacher, M. et al. Kelvin probe force microscopy. *Appl. Phys. Lett.* **58**, 2921–2923 (1991).
40. Kwon, S. Y. et al. Single Precursor Based Ultra-Low k Thin Film Deposited with Tetrakis(trimethylsilyloxy)silane in PECVD System. *Science of Advanced Materials* **10**, 1147–1153 (2018).
41. Yuhao, Z. et al. Threshold voltage control by gate oxide thickness in fluorinated GaN metal-oxide-semiconductor high-electron-mobility transistors. *Appl. Phys. Lett.* **103**, 033524 (2013).
42. Williams, R., Woods, M.H. Mobile fluoride ions in SiO₂. *J. Appl. Phys.* **46**, 695–698 (1975).
43. Shamiryan, D. et al. Low-K dielectric materials. *Materialstoday* **7**, 34–39 (2004).

Figures

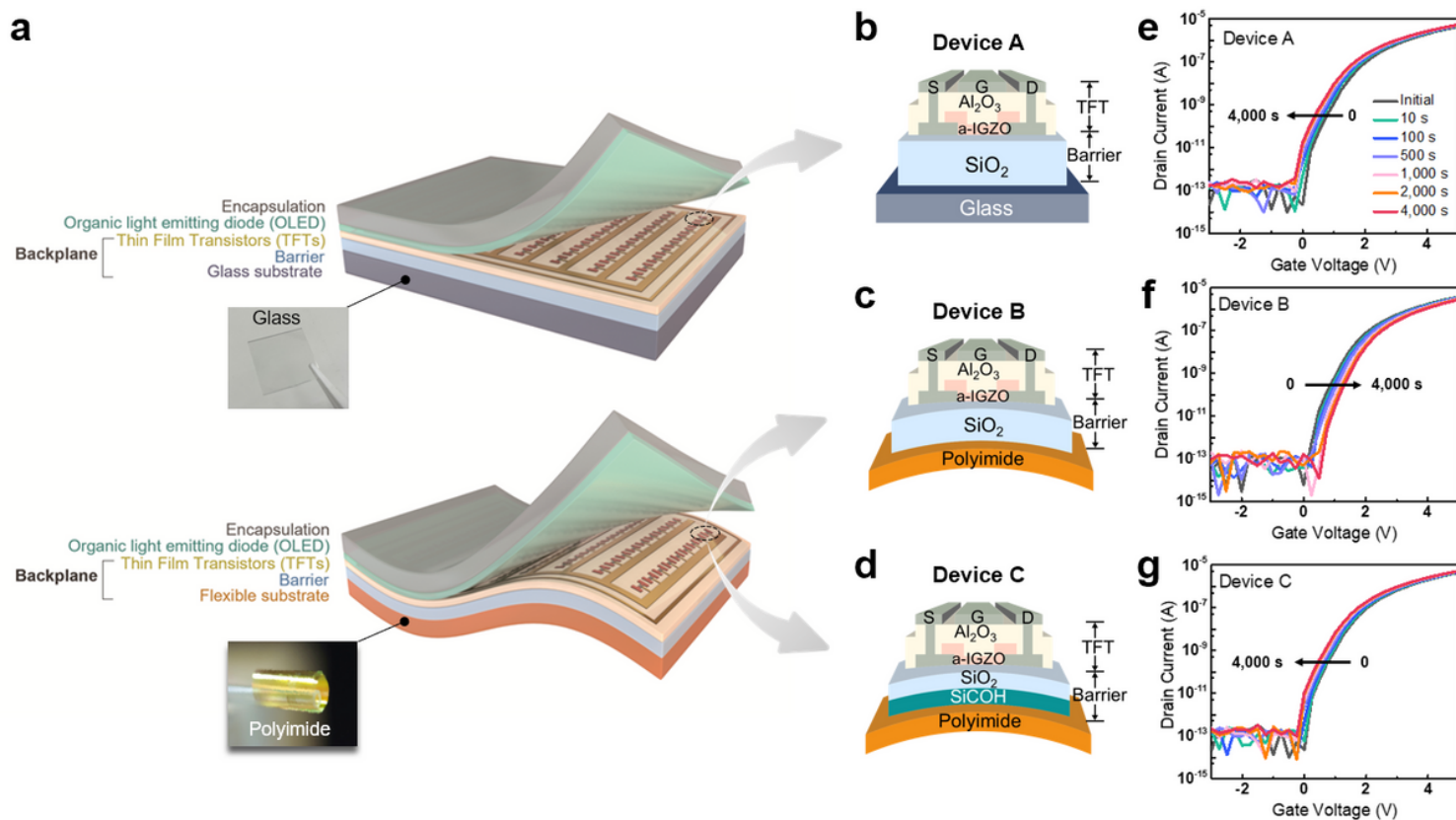


Figure 1

Device structure and electronic properties of a-IGZO TFTs. **a**, Stack structure of rigid display panel manufactured on glass substrate and flexible display panel manufactured on PI substrate. **b-d**, Schematic illustration of a-IGZO TFTs fabricated on SiO₂ barrier layer over the glass substrate, named as Device A and of a-IGZO TFTs fabricated on SiO₂ and SiO₂/SiCOH ($\epsilon = 2.40$) barrier layers over the PI substrate, named as Device B, and C, respectively. **e-g**, I-V characteristics of Device A, B, and C stressed under the NBTS test at 70 °C with -10 V gate voltage for 4,000 s. V_{th} shift by NBTS is -0.36 V for Device A, +0.45 V for Device B, and -0.25 V for Device C. Note that Device A and C show the negative V_{th} shifts. In contrast, a positive V_{th} shift is observed in Device B (The arrow in each graph indicates the direction of V_{th} shifts during NBTS).

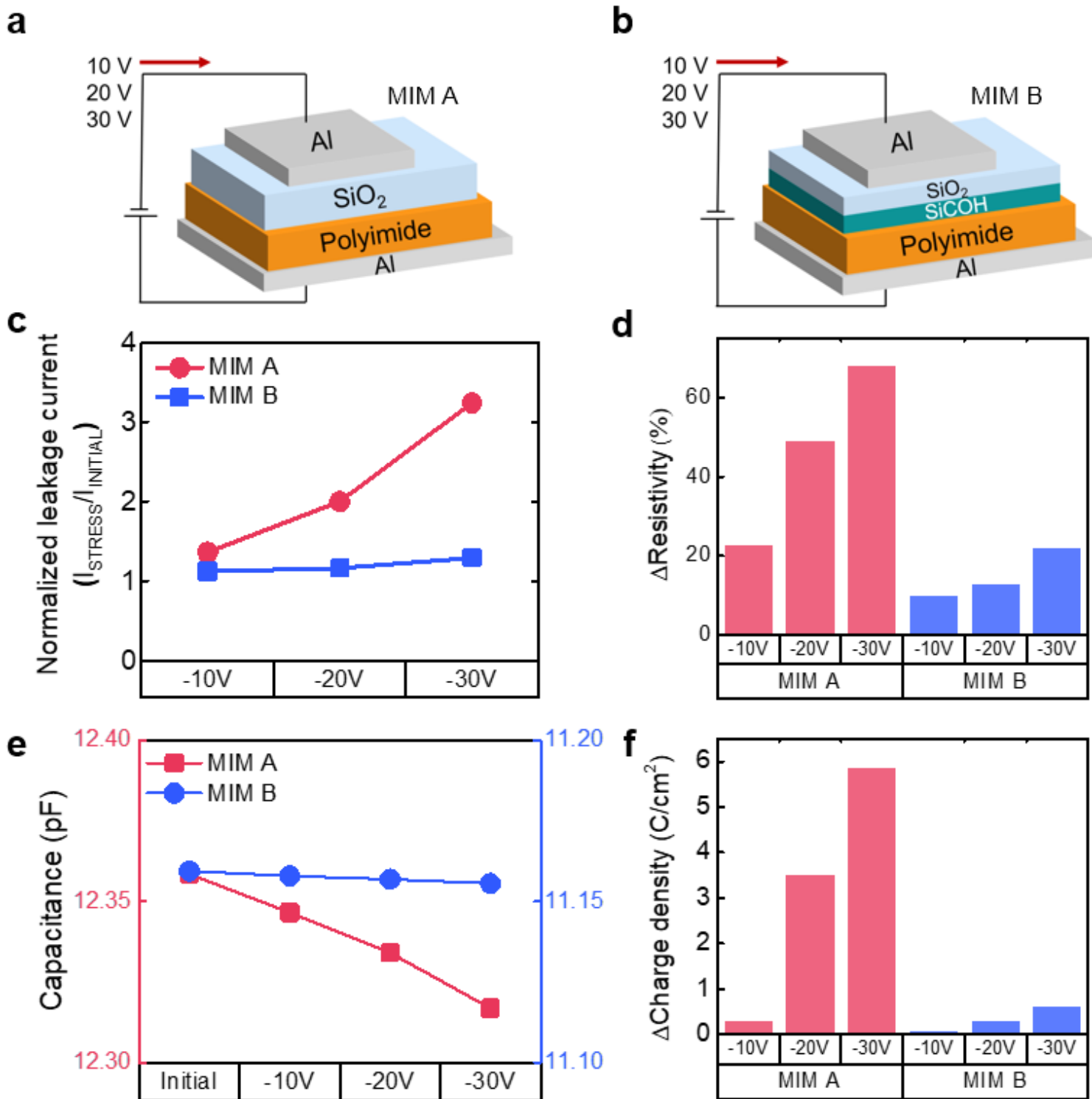


Figure 2

MIM capacitor and electrical characteristics. **a-b**, Schematics of MIM capacitor named MIM A (Al/SiO₂/PI/Al) and MIM B (Al/SiO₂/SiCOH/PI/Al). **c**, Plot of normalized leakage current based on the initial leakage current as a function of stress voltage. **d**, Changes in resistivity (%) extracted from the leakage current fluctuations of MIM capacitors. The thickness of the insulator was measured by SEM shown in Supplementary Fig. 1. **e**, Variation of capacitance (pF) of MIM capacitors due to voltage intensity. **f**, Changes in charge density (C/cm²) of MIM capacitors, as a function of stress voltage. Note

that MIM A and MIM B have 0.3 μm and 5 μm , and 0.15 μm and 5 μm , of SiO_2 and PI thickness, respectively.

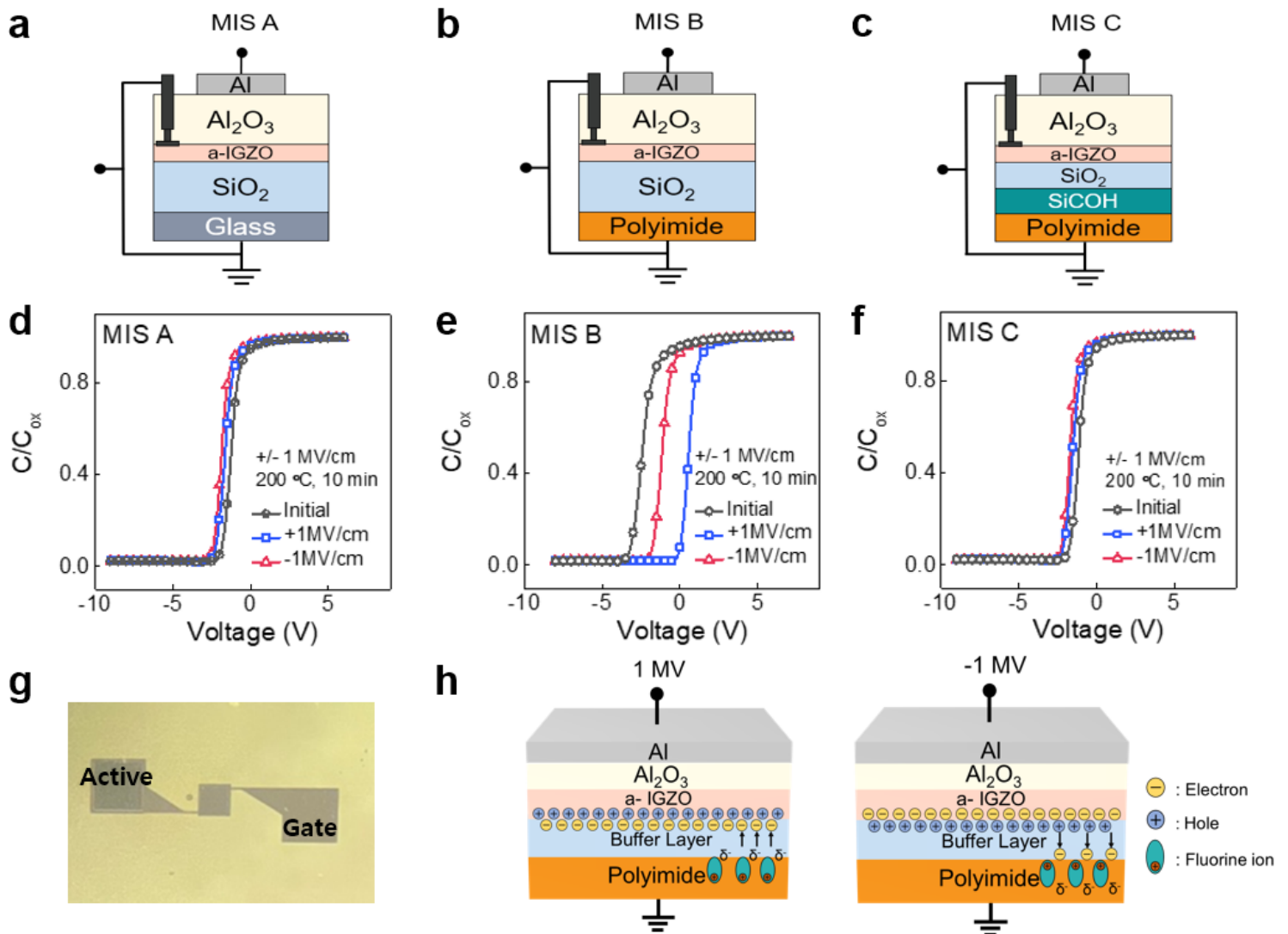


Figure 3

MIS capacitor and mobile charge of a-IGZO TFT device. **a-c**, Schematics of MIS capacitor fabricated with a-IGZO, SiO_2 , and SiCOH barrier layer over glass and PI substrate named as MIS A, B, and C, respectively. **d**, Stable performance of MIS A, Al/ Al_2O_3 /a-IGZO/ SiO_2 /glass substrate. **e**, Capacitance shifts of MIS B, Al/ Al_2O_3 /a-IGZO/ SiO_2 /PI substrate. **f**, Steady performance of MIS C, Al/ Al_2O_3 /a-IGZO/ SiO_2 /SiCOH/PI substrate, similar to MIS A. **g**, Photograph of MIS capacitor used for C-V measurement using voltage sweep from +1 to -1 MV/cm at 200°C for 10min. **h**, Illustration of mobile charging at SiO_2/PI interface responsible for higher capacitance change observed for MIS B shown in f.

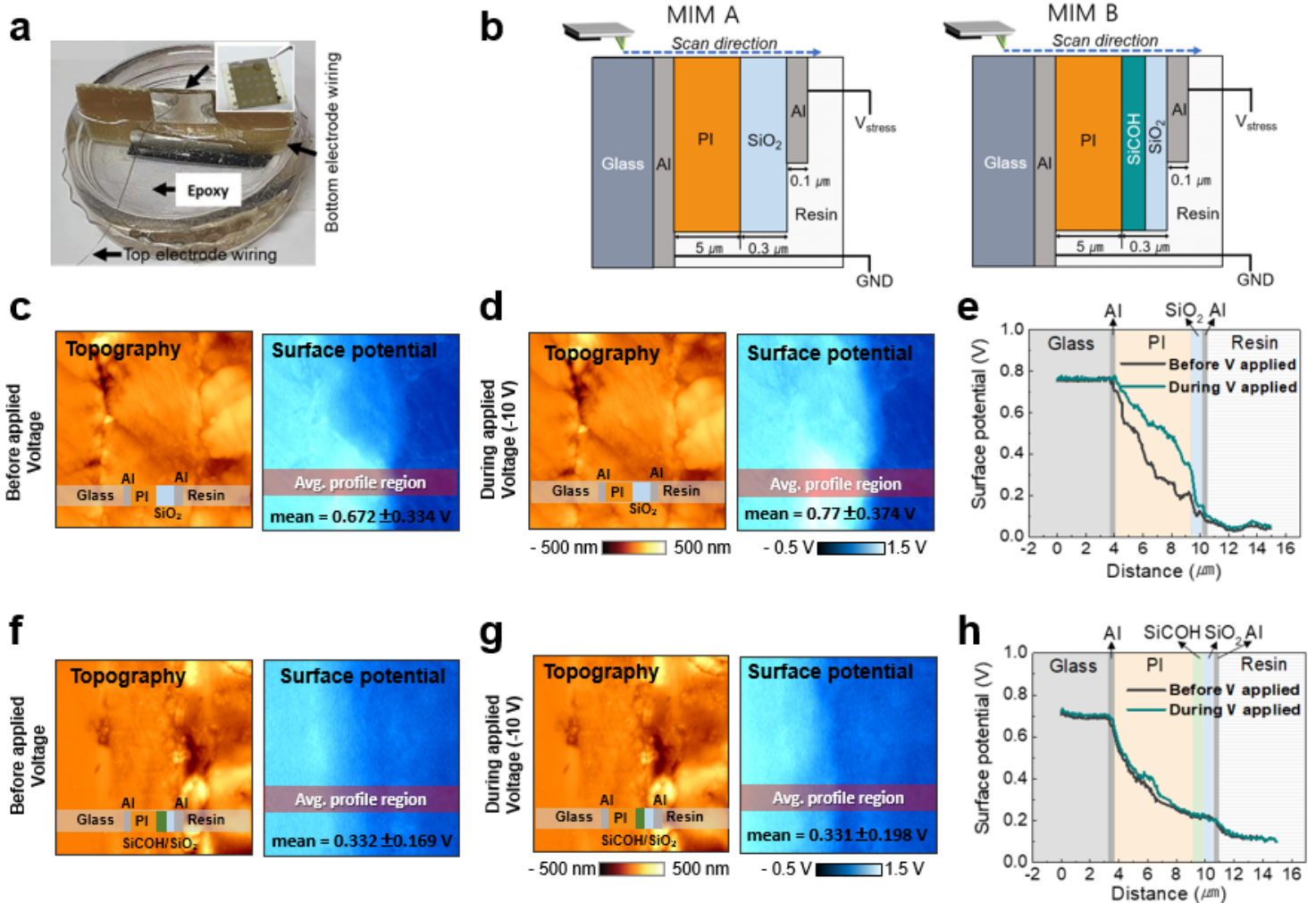


Figure 4

KPFM analyses and surface potential measurement. **a**, Photograph of the MIM capacitor fabricated on the glass substrate prepared for KPFM measurement (MIM capacitor is molded with an epoxy). **b**, Schematics of the MIM capacitor and KPFM scanning direction. MIM capacitors were cross-sectioned for surface scanning from glass to resin (scan length 15 mm). **c-e**, MIM A: KPFM topography and surface potential. **f-h**, MIM B: KPFM topography and surface potential, before and after the applied voltage of -10 V. KPFM enables the AFM topography and surface potential to be simultaneously measured.

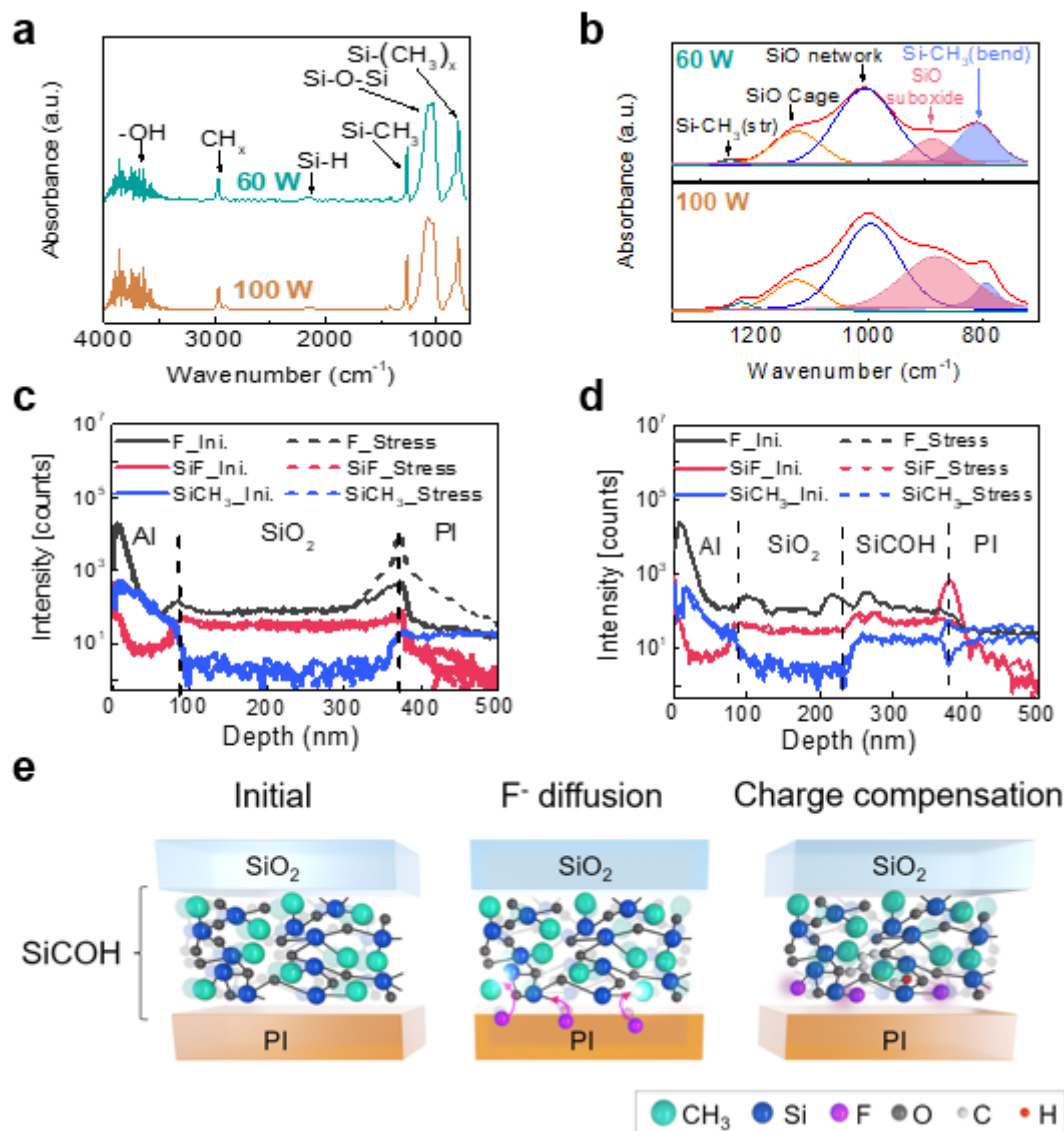


Figure 5

Physical characterization and PI charging compensation mechanism of the SiCOH layer. **a**, FT-IR absorption spectra of the SiCOH layer with different plasma powers. **b**, FT-IR spectra of SiCOH with silicon-related peak fitting. **c-d**, Analysis of F^- mobile charge by SIMS on MIM A (Al/ SiO_2 /PI/Al) and B (Al/ SiO_2 /SiCOH/PI/Al) capacitor, respectively. **e**, Schematic diagram of charge compensation mechanism of SiCOH layer between PI and SiO_2 . F^- generated from PI substrates and trapped between PI and SiO_2 interface under NBTS and the ionized fluorine is neutralized by bonding with the SiCOH layer.

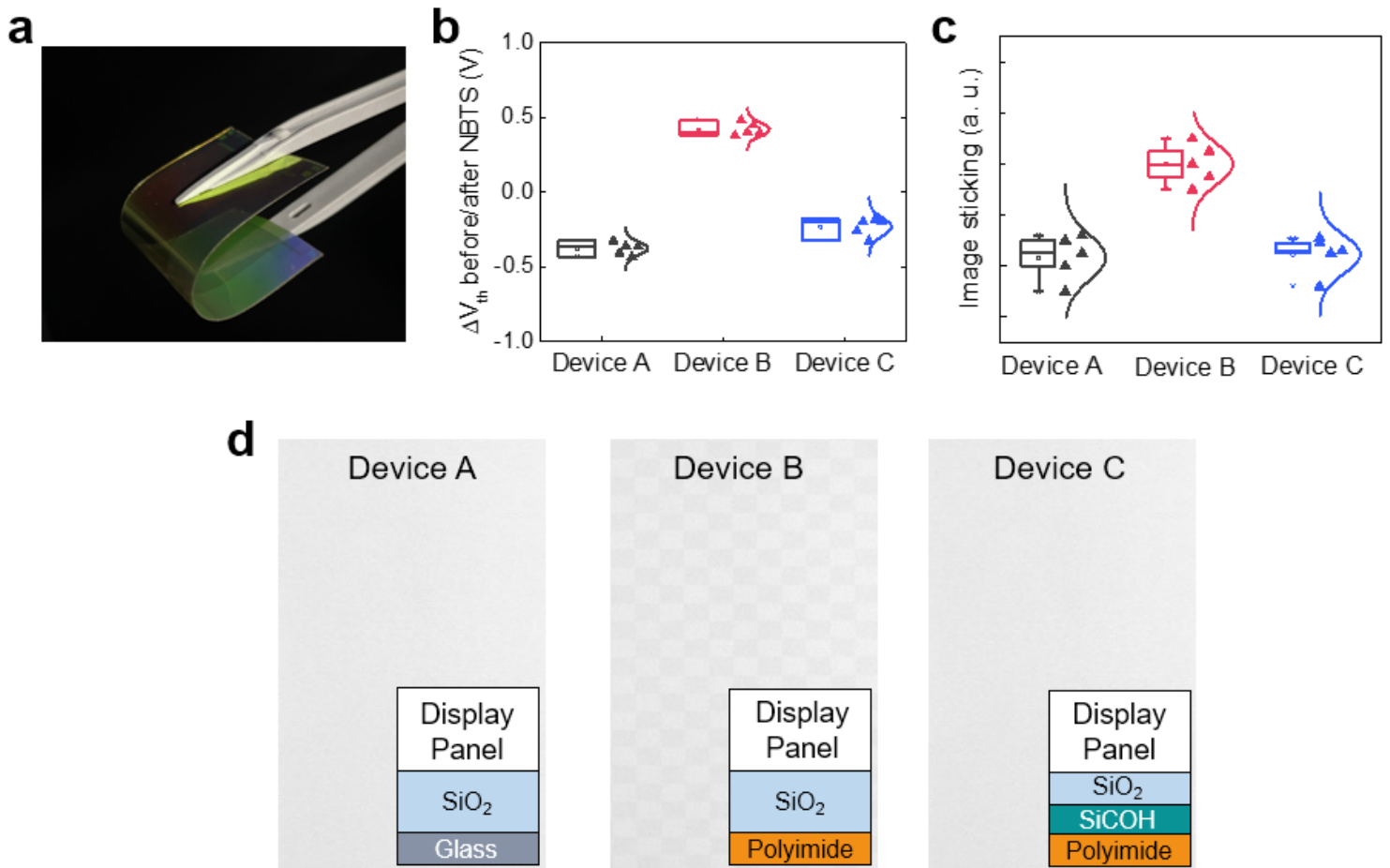


Figure 6

Flexible device and reliable display and performance. **a**, Photograph of a flexible OLED panel manufactured on PI substrate. **b**, ΔV_{th} shifts of Devices A, B, and C before and after NBTS conditioned at 70 °C for 4,000 s with -10 V gate voltage. **c**, Image sticking performance measured by flexible panels of Device A, B, and C (the sample size for each device is 5). The image sticking performance becomes better when the index lowers. **d**, Image sticking evaluation results of three flexible OLED display panels with different backplane structures. Devices A and C (the panels with the glass and PI using SiCOH charge compensation layer) show less image sticking phenomena than Device B (the panel with the PI substrate using SiO₂, without SiCOH layer).

Supplementary Files

This is a list of supplementary files associated with this preprint. Click to download.

- [Supplementaryinformation.docx](#)